A cysteine-based redox switch regulates millisecond dynamics of PDI and controls enzyme activity

Mathivanan Chinnaraj[1], Robert Flaumenhaft[2,*] and Nicola Pozzi[1,*]

[1]*Edward A. Doisy Department of Biochemistry and Molecular Biology, Saint Louis University School of Medicine, St. Louis, MO, 63104, USA.*

[2]*Division of Hemostasis and Thrombosis, Department of Medicine, Beth Israel Deaconess Medical Center, Harvard Medical School, Boston, Massachusetts 02115, USA.*

*Corresponding authors:

Robert Flaumenhaft
Email: rflaumen@bidmc.harvard.edu
Phone: +1-617-735-4005

Nicola Pozzi
Email: nicola.pozzi@health.slu.edu
Phone: +1-314-977-9241

Keywords: single-molecule FRET, protein dynamics, thiol-oxidoreductases, chaperones, protein disulfide isomerase, thrombosis

Abstract

Cysteine residues provide enzymes involved in signaling and metabolism with an allosteric mechanism to quickly respond to changes in the surrounding redox environment. Yet how thiol modifications impact enzyme structure and dynamics is poorly understood. Here, we apply single-molecule Förster resonance energy transfer (smFRET) to study redox-dependent conformational dynamics of a highly flexible oxidoreductase, protein disulfide isomerase (PDI), in solution. We demonstrate that PDI toggles in the millisecond timescale between two major conformational ensembles, “open” and “closed”, that differ ~20Å in length due to relocation of the two catalytic domains, whose equilibrium distribution is modulated by the redox state. While reduced PDI predominantly populates the open ensemble, oxidized PDI visits both ensembles with similar probability. We provide evidence that i) transition from the open to the closed ensemble requires loss of free thiols, not disulfide bonding, as previously thought, and ii) exposure to small molecules that alkylate the catalytic cysteines and mutation of cysteines in the N-terminal active site shift PDI to the closed conformation. Finally, using mutational and kinetic analyses, we show that the fraction of open ensemble at equilibrium positively correlates with the reductase activity of PDI. This work forms the basis of a new dynamic mechanism of PDI regulation by a cysteine-based redox switch in which thiol-controlled equilibrium distribution of the open/closed ensembles dictates function.

Introduction

Due to the unique chemistry of the sulfur-containing sidechain, cysteine residues serve important functions in enzymatic catalytic sites and in regulatory aspects of enzyme function (1, 2). Depending on the redox state, cysteines can carry out multiple chemistries, such as oxidation and reduction, and, by forming disulfide bonds, can allosterically modify an enzyme conformation, thereby altering enzyme activity (3). As a result of this chemical versatility, cysteine-based redox switches are increasingly recognized as important regulators of enzyme function (1) as they provide a rapid yet very precise mechanism for spatiotemporal regulation of redox-sensitive enzymes (2).

While a plethora of biochemical data demonstrates that the redox microenvironment is mostly responsible for determining the type of catalytic activity of a cysteine-based enzyme, how redox changes of cysteine residues influence enzyme structure and dynamics remains poorly understood. In this context, protein disulfide isomerase (PDI) represents a biologically relevant model system, which lies at the interface between basic (4, 5) and translational science (6, 7). PDI is an archetypal oxidoreductase capable of forming new disulfide bonds and breaking existing ones in hundreds of client proteins (8), thus regulating development (7), cell growth (9, 10), innate and adaptive immunity(11-13), and hemostasis (6, 14, 15). It comprises 508 amino acids organized in four thioredoxin domains arranged in the order **a**, **b**, **b'** and **a' (Figure 1A)** connected by three flexible linkers**.** Domains **a** and **a'** contain the catalytic motif CGHC, whereas the **b** and **b'** domains are thought to be responsible for substrate and cofactor recruitment (16-18). In the oxidized form (S-S), the vicinal cysteines form a disulfide bond, thus promoting oxidation of a dithiol incoming substrate. By contrast, in the reduced form, free thiols (-SH) reduce a substrate disulfide bond and become oxidized in the process.

Over the past two decades, structural, computational, and biophysical studies have documented large-scale redox-dependent conformational changes in the human enzyme and orthologs (16, 19-23). However, elucidation of the intimate relationship between domain fluctuations and catalysis has remained challenging due to several technical limitations. Although easily accessible, ensemble methods are difficult to interpret on a structural basis since the signal is averaged over multiple conformations, preventing direct identification of distinct functional states. X-ray crystallography and single-molecule imaging techniques that require tethering of flexible proteins onto a surface may impose constraints on structural variability and, as in the case of high-speed atomic force microscopy (HS-AFM) and traditional camera-based total internal reflection fluorescence (TIRF) microscopy, do not have the temporal resolution to observe microsecond kinetics. Multidimensional nuclear magnetic resonance (NMR) experiments, although ideal, are greatly complicated by the relatively large size of PDI (i.e., 58 kDa).

To complement current studies and advance our fundamental understanding of this medically relevant enzyme, here we apply confocal single-molecule FRET (smFRET), a technique with high temporal resolution (24-28), to study the redox-dependent conformational dynamics of PDI in solution. We provide evidence that PDI toggles in the millisecond timescale between two major conformational

ensembles, “open” and “closed”, that differ due to the relocation of the two catalytic domains. We show that the redox microenvironment modulates this pre-existing equilibrium without, however, forming new macroscopic species. Finally, we document that while stabilization of the open ensemble requires a catalytically competent N-terminal active site and coordinated interactions between domains, transition from the open to the closed ensemble simply requires loss of free thiols, not disulfide bonding, as previously thought (23). These findings form the basis of a new dynamic mechanism of PDI regulation in which thiol-controlled equilibrium distribution of the open/closed ensembles dictates function. Given the structural similarities between PDI and other oxidoreductases (8), this regulatory mechanism may extend to other family members and, more generally, to other cysteine-based enzymes.

Results

Experimental design and site-specific labeling of catalytically active PDI. The X-ray crystal structures of oxidized (S-S) and reduced (-SH) PDI obtained in the absence and presence of 50 mM 1,4-Dithiothreitol (DTT) as a reducing agent (16) are shown in **Figure 1B**. They document a flexible U-shape architecture and large redox-dependent conformational changes involving the relocation of the two catalytic domains facing each other. Specifically, oxidized PDI is significantly more “open” as compared to reduced PDI (“closed”) and this is demonstrated by the distance between the catalytic sulfur atoms C53 in the **a** domain and C397 in the **a´** domain, which varies from 40.3 Å in oxidized PDI to 27.6 Å in reduced PDI. Since closing of the active site cleft in the structure of reduced PDI limits the accessibility of the substrate-binding pocket in the **b’** domain, it is currently believed that, while the open form of oxidized PDI is primed for substrate binding, inward movements of the **a** and **a’** domains due to reduction of the active site cysteines are responsible for substrate release and enzyme regeneration **(Figure 1C)** (5, 16, 23).

To track the conformational reengagements of the **a** and **a’** domains captured by X-ray crystallography in **Figures 1B** and summarized in **Figure 1C** and define the interconversion rate between the open and closed states in solution, we designed the FRET sensor 88/467. This pair was selected for the following reasons. First, residues S88 and K467 are exposed to the solvent and located >10 Å away from the active sites, thus minimizing the possibility of functional and structural perturbations resulting from the incorporation of the fluorescent dyes. Second, our structure-based calculations based on **Figure 1B** predict significantly higher values of energy transfer, 0.29 units, when PDI transition from the oxidized (0.67) to the reduced (0.97) state.

Given that PDI’s active sites contain cysteine residues, donor (Atto550) and acceptor (Atto647N) fluorophores were specifically introduced at positions 88 and 467 using biorthogonal chemistry by following a procedure recently developed and validated in our laboratory (29). After purification, doubly labeled PDI 88/467 was properly folded, as documented by far-UV CD and intrinsic fluorescence **(Figure S1)**, catalytically active, as shown by the ability of the labeled protein to reduce insulin with rates

comparable to the unlabeled protein and PDI WT **(Figure S1)**, and had fully oxidized active sites, as judged by the lack of reactivity toward a maleimide dye **(Figure S1).** Importantly, dyes at positions 88 and 467 also made no significant interactions with the protein and can therefore be considered freely rotating in solution. This was demonstrated by measuring the values of anisotropy and quantum yield for donor only and acceptor only PDI molecules **(Table S1)**.

Rapid conformational dynamics of PDI revealed by smFRET. smFRET studies of PDI were performed using a confocal microscope. The fluorescence intensity and lifetime of labeled PDI at 100 pM concentration were simultaneously measured as molecules freely diffuse through the confocal volume (i.e., ~1 ft). Fluorescence bursts with >40 photons were used to calculate FRET efficiency values. Histograms were created from thousands of events using five independent protein preparations. Given that the Förster Radius (R_0) of the FRET couple Atto-550/Atto-647N is ~65Å, interprobe distances from ~40 to ~90Å are measured.

The FRET efficiency histograms of PDI 88/467 obtained in the absence (top panel) and presence (bottom panel) of 1 mM DTT are reported in **Figure 1D**. Two important findings emerged from the analysis of these plots. First, we documented that oxidized PDI 88/467 is very responsive to DTT's addition, displaying a large shift of the signal toward lower FRET values. This result corroborates our recent observations (29) and demonstrates that the probes at positions 88 and 467 are ideally located to track the movements of the catalytic domains with high temporal resolution. It is important to note, however, that, while useful for designing the FRET pair 88/467, the structures in **Figures 1B** explain neither the findings obtained here with the FRET pair 88/467 **(Figures 1E)** nor previously published data with the FRET pairs 42/467 and 308/467(29), suggesting that the two-state model of PDI regulation proposed earlier needs revision. Second, we noticed that dyes positioned at residues 88/467 displayed board FRET distributions in both redox states, implying substantial conformational heterogeneity of PDI in solution. While some degree of conformational heterogeneity was expected in oxidized PDI based on very recent HS-AFM experiments (23), it was not anticipated for reduced PDI. The FRET data, therefore, provide clear-cut evidence that PDI adopts multiple conformations in solution regardless of the redox state and on the millisecond timescale. Consistent with this interpretation, a satisfactory fit of the FRET data was obtained with a dynamic two-state model, which predicts that the exchange between two macroscopic ensembles with distinct FRET efficiencies occurs while single molecules diffuse through the confocal volume, which is 0.5-1 ms. Using this model, reduced PDI was found to predominantly (~95%) adopt a low FRET state centered at E=0.51 and a minor high FRET state center at E=0.91 (~5%). By contrast, oxidized PDI was more evenly distributed between low (~60%) and high (~40%) FRET states. Since lower FRET values indicate larger distances between the fluorescent dyes whereas higher FRET values correspond to a closer positioning of the dyes, we named these two conformational states of PDI "closed"

and “open”, to keep it consistent with the design conceptualized based on the crystal structures shown **Figure 1B**.

The assumption that PDI molecules undergo rapid conformational dynamics unfolding in the millisecond timescales is not trivial and needs independent validation. To this end, we constructed a plot in which the FRET efficiency of PDI 88/467 was graphed versus the fluorescence lifetime of the donor in the presence of the acceptor ($\tau_{D(A)}$) of each molecule. In this plot, as demonstrated elsewhere (30, 31), interconversion between FRET states appears as a systematic deviation of the experimental data from the so-called “static” FRET line, which is the line that describes the theoretical relationship between the values of $\tau_{D(A)}$ and the values of energy transfer. For oxidized PDI 88/467 **(Figure 2A)**, a systematic deviation from the static FRET line connecting two distinct populations characterized by lifetime values of ~0.35 and ~1.59 ns was clearly visible in the plot. These two FRET populations, in agreement with our dynamic two-state model, correspond to FRET efficiency values of ~0.90 and ~0.50. For reduced PDI **(Figure 2D)**, the bridge was not visible with the same counter-level values used for oxidized PDI simply because of the low abundance (5%) of the high FRET population.

Even though a dynamic two-state model provided a satisfactory explanation of the FRET data, a more careful analysis of the 2D-lifetime plots revealed that the center of the open ensemble did not reside on the static FRET line but was significantly shifted toward the right. This indicates that rapid dynamics exist within the open ensemble (32). To investigate this new observation further, we performed two experiments. First, we isolated the bursts from the FRET interval 0.25-0.65 and performed subpopulation specific fluorescence lifetime analysis. The best fit was obtained with a double exponential function, with τ_1=1.12±0.2 ns and τ_2=2.25±0.3 ns, corresponding to two distinct FRET states with values of ~0.35 and ~0.70, which we called O_1 and O_2 **(Figure 2C)**. Second, we analyzed trajectories of individual PDI molecules longer than 2 ms that were binned at 200 μs. Anticorrelated donor/acceptor signals were detected in a few of them, providing further evidence of two states at equilibrium **(Figure 2D)**, which according to our simulations **(Figure S2)** and previously reported data for a dynamic two-state model similar to ours (33, 34), exchange faster than 1 ms^{-1} but slower than 10 ms^{-1}. Hence, the open ensemble appears as one broad FRET distribution when PDI 88/467 is binned at 0.5 ms because O_1 and O_2 exchange faster than 1 ms^{-1}. The rapid exchange between these two states also explains why a dynamic two-state model provides a good snapshot of the distribution between open and closed ensembles at equilibrium.

To summarize, smFRET measurements of PDI 88/467 provide evidence that PDI toggles in the millisecond timescale between the two major conformational ensembles, “open” and “closed”, whose equilibrium distribution is modulated by the redox environment. The open ensemble, however, is very dynamic and comprises two states, O_1 and O_2, that interconvert more rapidly in the microsecond timescale.

Loss of free thiols, not disulfide bond formation, mediates stabilization of the oxidized state. PDI has two active sites, one in the N-terminal **a** domain (C53/C56) and another in the C-terminal **a'** domain (C397/C400). Our data have shown that reduced and oxidized PDI adopt multiple conformations at equilibrium and that addition of a reducing agent is necessary and sufficient to trigger major redox-dependent conformation changes involving relocation of the catalytic domains. A role for disulfide bond formation between catalytic cysteines in the active site motif has previously been proposed to control redox-mediated conformational changes. However, this premise is unproven. To address this point, all four catalytic cysteines were substituted with the redox-insensitive amino acid alanine to generate the quadruple mutant PDI 88/467/C53A/C56A/C397A/C400A, named hereafter PDI-AA/AA. After having verified that PDI-AA/AA was catalytically inactive **(Figure S3)**, smFRET measurements were collected in the absence and presence of DTT, as described previously. Remarkably, we found that PDI-AA/AA was very similar to oxidized PDI 88/467 and insensitive to the addition of DTT **(Figure 3A)**, implying that this variant is incapable of achieving a reduced conformation. Moreover, the similarity between PDI-AA/AA and oxidized PDI 88/467 implies that the loss of free thiols, and not disulfide bonding, is the underlying mechanism responsible for shifting the equilibrium towards the closed ensemble. If disulfide bonding stabilized the oxidized state, PDI-AA/AA should have been similar to reduced PDI 88/467. Further validation to this conclusion came from an experiment in which we monitored, in real time, the reaction between reduced PDI and the irreversible active site inhibitor 16F16 (35) **(Figure 3B)**. By eliminating the free thiol groups from the active sites (35), 16F16 shifted the equilibrium toward the closed ensemble **(Figure 3C)**, as expected. Similar results were obtained with PACMA-31 **(Figure S4)**, which is another commonly used active site inhibitor of PDI (36).

Having established that free thiols are important for stabilizing the open ensemble, we next evaluated the contribution of each active site. To this goal, we produced two new variants lacking either the C-terminal C397/C400 (PDI 88/467/C397A/C400A or PDI-CC/AA, **Figure 4A**) or N-terminal C53/C56 (PDI 88/467/C53A/C56A or PDI-AA/CC, **Figure 4B**) catalytic motifs. We found that FRET profiles of the two variants were very similar to each other under oxidizing conditions and almost identical to PDI 88/467. However, they showed significant differences in the presence of DTT. Specifically, while PDI CC/AA behaved like PDI 88/467, an intermediate behavior was seen for PDI AA/CC insofar as the transition from the oxidized to the reduced state was incomplete, leading to a substantial (>3 times more, from 5% to 18%) accumulation of closed ensemble. Importantly, this latter phenomenon was not caused by a reduced reactivity of PDI AA/CC toward DTT since the closed ensemble never disappeared, even at very high (50 mM) concentrations of DTT. Hence, this data indicates that a catalytically active N-terminal active site is necessary and sufficient to stabilize the open ensemble in response to DTT.

The observation that reduced PDI mostly visits the open ensemble and that free thiols in the N-terminal active site stabilize the open ensemble merits further attention, especially in the context of PDI's enzymatic activity. This model predicts that the destabilization of the open ensemble in PDI AA/CC may

lead to lower reductase activity. To test this hypothesis, we measured the reductase activity of PDI 88/467 and the active site variants towards the fluorogenic substrate di-eosin-GSSG **(Figure 4C and 4D)**. In contrast to larger macromolecular substrates like insulin, di-eosin-GSSG is smaller and interacts solely with the active sites (37), thus facilitating the interpretation of the kinetic results. While no enzymatic activity was observed for PDI AA/AA, as expected, both PDI CC/AA and PDI AA/CC were active towards di-eosin-GSSG. However, while the PDI CC/AA mirrored the activity of PDI 88/467, PDI AA/CC was compromised, displaying a dramatic 7-fold reduction of the catalytic activity. Importantly, this effect was due to a reduction of k_{cat} and not K_M, documenting the allosteric nature of this functional perturbation. It has been demonstrated before that **a** and **a'** have similar enzymatic activities when isolated from the rest of the molecule (38).

PDI's conformational dynamics explain ALS-linked loss of function mutation R300H. To further investigate the validity of our model and explore its functional significance in the context of physiology, we mutated residue R300 in the **b'** domain and residue W396 in the **a'** domain to histidine and alanine, respectively, into the 88/467 background **(Figure 5)**. This is because previous structural studies have shown that residue W396 synergistically works with residue R300 to stabilize the closed state of PDI (16, 23, 39). Furthermore, the loss of function mutation R300H has been reported to cause motor dysfunction, and it is therefore linked to the early onset of amyotrophic lateral sclerosis (ALS) (40). After expression and purification, we first verified that, in the 88/467 background, the mutations R300H and W396A caused the same macroscopic effects documented before in the wild-type background. To this end, we performed the insulin reductase activity assay and limited proteolysis experiments using proteinase K. Consistent with published data (39, 40), the reductase activity of both variants was compromised **(Figure 5A)**, and cleavage of R300H and W396A by proteinase K occurred faster compared to PDI wild type **(Figure 5B)**. We then performed smFRET and kinetic experiments, as done beforehand for the active site variants. Using smFRET, we found that the mutations R300H **(Figure 5C)** and W396A **(Figure 5D)** caused a significant redistribution of the FRET signal PDI toward higher FRET values. This indicates that residues R300 and W396 are important for stabilizing the open ensemble, and not the closed, as proposed before (16, 23, 39). Furthermore, since proteinase K cleaves residues M356 in the **x**-linker region (41), our data indicate that the **x**-linker is more susceptible to proteolysis when PDI adopts a closed conformation. It was also interesting to observe that the perturbation introduced by the mutation W396A was more profound than the effect caused by the mutation R300H, suggesting that, in the open forms, these two residues may be part of an extended allosteric network rather than interacting with each other. Finally, in our kinetic assays, we determined that both R300H and W396A had compromised reductase activity and that the values of k_{cat} increased linearly when plotted against the fraction of open ensemble at equilibrium **(Figure 5F)**. This supports the idea that the equilibrium distribution of the open/closed ensembles dictates function.

Discussion

PDI is an exceptionally flexible protein capable of adopting multiple conformations in response to the redox environment and small molecules (22). Crystallography and biophysical techniques have provided invaluable insights regarding redox-dependent conformational changes of PDI. Such approaches, however, fail to capture the full range of structural dynamics that occur in solution and on the microsecond scale. Our results indicate that the protein energy landscape of PDI is dynamic and that such rapid conformational fluctuations are critical determinants of its function.

By applying smFRET, we found that PDI toggles between two major conformation ensembles at equilibrium whose distribution is modulated by the redox environment. Measurements using freely rotating dyes located at positions 88/467 indicate a movement of approximately ~20Å as PDI converts back and forth between closed and open ensembles. Using different analyses, we determined that the rate at which these two ensembles interconvert is in the millisecond timescale. Even though future studies will be necessary to elucidate the exact kinetic scheme and precisely measure the states' interconversion rate constants, this finding is very informative from a mechanistic standpoint. Since millisecond large-scale domain movements are compatible with substrate binding kinetics (25, 42-44), these spontaneous fluctuations of the catalytic domains may serve as a gating mechanism that PDI exploits to distinguish between different types of protein substrates and carry out alternative enzymatic reactions. For example, structures within the open ensemble with a wider cavity could prefer larger protein substrates. In contrast, structures in the closed ensemble with a narrower cavity may represent a resting state of the enzyme or interact with smaller ligands such as unfolded polypeptide chains lacking tertiary structure. PDI's ability to spontaneously interconvert between these two ensembles at equilibrium could also provide the structural basis for its chaperone activity, which does not require catalytic activity but simply structural integrity of the oxidized state (39).

Previous X-ray structural data of PDI have been instrumental in proposing a model of PDI-assisted catalysis whereby compaction and rigidification of the enzyme upon reduction limit the exposure of the hydrophobic pocket in the **b'** domain, thus explaining substrate binding, processing, and release (5, 16, 23). Evaluation by smFRET of PDI reduced with DTT led to two discoveries that challenge this model. First, reduced PDI unexpectedly demonstrated structures in which residues 88/467 are substantially more distant than what is predicted by X-ray crystallography (16). This observation demonstrates that, in solution, the reduced state is not as compact as previously thought. Second, we discovered that the reduced form of PDI is very dynamic as it shuffles between O_1 and O_2 conformations with exchange rates in the microsecond timescale **(Figure 2)**. Since these motions are faster than substrate binding kinetics, like in other allosteric enzymes, they may finely tune enzyme catalysis by allowing the protein to optimally adjust the position of the catalytic motifs while a substrate is bound (24, 26). Alternatively, they could enable fast crossing between two "energetically frustrated" enzyme conformations with different catalytic activities (45, 46)

The discovery that the reduction of PDI redistributes its conformational landscape towards the open ensemble raises important questions as to the molecular mechanism by which PDI couples the chemistry of the active sites with changes in its conformation and how the signal is propagated throughout the molecule. A recent study showed that mutation of the catalytic cysteine residues with alanine mimics the reduced form (23), suggesting that disulfide bonds stabilize the oxidized state. Another study showed that catalytically inactive PDI in which the catalytic cysteine residues were mutated to serine retained chaperone activity similar to oxidized PDI but different from reduced PDI (39). According to the smFRET results with the catalytically inactive mutant PDI-AA/AA **(Figure 3A)** and the small molecule inhibitor 16F16 **(Figures 3B and 3C)**, we solve this conundrum and demonstrate that the chemical trigger initiating redox-dependent conformational changes is the presence of free thiol groups and not disulfide bonding. Given that the catalytic motif CxxC is present in many members of the PDI family (8), this mechanism may be conserved in other oxidoreductases.

In conclusion, a new model for the PDI conformational dynamic cycle that challenges current postulates in the field emerges from these studies **(Figure 6A)**. In contrast to a static two-state model of PDI regulation in which major conformational changes are triggered by the redox environment, we propose that oxidized PDI spontaneously samples open and closed ensembles at equilibrium, and such equilibrium is important for substrate recognition. After transferring the disulfide bond to the substrate, PDI becomes reduced, and new thiol groups are generated. This acts as a molecular switch that redistributes the conformational landscape of the enzyme toward the open ensemble, thus facilitating substrate-induced dimerization (23) and enzyme regeneration. Naturally occurring mutations, like those found in ALS patients (40) **(Figure 6B)**, and chemical modifications of the active sites that eliminate free thiols (4), like alkylation **(Figure 3)**, and perhaps S-nitrosylation, and sulfenylation, perturb this allosteric equilibrium, thus modulating PDI activity.

Materials and Methods

Protein production and purification. The cDNA of human PDI (residues 18-479) was cloned into a pBAD vector expression system (ThermoFisher) and modified to include an N-terminal 6 his-tag and a C-terminal Avitag. Genetic incorporation of the unnatural amino acidic N-Propargyl-L-Lysine (Prk) (SiChem) at positions 88 and 467 was obtained using the AMBER suppressor pyrrolysine tRNA/RS system from *Methanosarcina mazei*. Mutations C53A, C56A, C397A, C400A, R300H and W396A in the 88/467 background were generated using the Quickchange Lightning kit (Agilent) with appropriate primers. Sequence verified PDI variants (Genewiz) were expressed in Top10 cells and purified following recently published procedures (29).

Protein labeling. Site-specific labeling of PDI 88/467 and variants was achieved by reacting 25 μM of PDI in phosphate buffer saline (PBS) pH 7.4 with 4x molar excess of azide dyes (donor, acceptor or

donor/acceptor mixtures) (Sigma-Aldrich) in the presence of 150 μM copper sulfate ($CuSO_4$), 750 μM tris-hydroxypropyltriazolylmethylamine (THPTA), and 5 mM sodium ascorbate. The reaction mixer was left on slow rotisserie for 1 hour 30 minutes at room temperature, then 30 minutes on ice. Monomeric PDI was successfully separated by protein aggregates by size exclusion chromatography (SEC), using a Superdex 200 10/300 column (Cytiva) equilibrated with Tris 20 mM (pH 7.4), 150 mM NaCl, 2 mM EDTA. The quality of each protein preparation was assessed by NuPAGE Novex 4–12% Bis-Tris protein gels (ThermoFisher). Gels were stained with Coomassie Brilliant Blue R-250 (ThermoFisher) and scanned on a Typhoon imager (Cytiva) at 532 nm and 633 nm to verify specific incorporation of the fluorescent dyes. Total protein concentration was determined by reading the absorbance at 280, using a molar coefficient adjusted for the amino acidic sequence of each variant. The concentration of Atto-550 and Atto-647N was calculated by reading the absorbance at 550 nm and 640 nm, respectively. Typical labeling efficiencies were 90%.

Di-eosin-GSSG disulfide reductase assay. The probe di-eosin glutathione disulfide, di-eosin-GSSG, was purchased by Cayman Chemical and its enzymatic cleavage by PDI was monitored in a 96-well fluorescence plate format as described earlier (37). Briefly, a solution of PDI (100 μl, 30 nM) solubilized in PBS containing 2 mM EDTA was first incubated for 30 minutes at room temperature with 100 μM DTT to ensure complete reduction of the enzyme and then added to a solution (100 μl) of di-eosin-GSSG. The increase in fluorescence due to di-eosin-GSSG cleavage was monitored for 20 min in a Spectramax i3 spectrofluorometer (Molecular Devices) at 550 nm, after excitation at 520 nm. Eight-point response curves were generated for each titration using a range of different di-eosin-GSSG concentrations (0.15–20 μM). Each titration was repeated three times. Enzyme kinetics analysis was performed using Origin 2015 (OriginLab).

Insulin reductase assay. PDIs (400 nM) were solubilized in PBS and then added to a solution containing 0.2 mM human insulin (Sigma-Aldrich), 2 mM EDTA and 325 μM DTT. The reaction was monitored at 650 nm (turbidity due to precipitation of the product) for 1 h at 25 °C using a Spectramax i3 (Molecular Devices).

Digestion with Proteinase K. PDI 88/467 and mutants R300H and W369A were dissolved in 20 mM Tris, 145 mM NaCl, 2 mM EDTA, pH 7.4, 1 mM DTT at 1 mg/ml (60 μl). Following the addition of proteinase K (Sigma-Aldrich) (final concentration 5 μg/ml) aliquots (16 μl) were quenched at different time intervals with 1 mM PMSF (2 μl) for 2 minutes at room temperature before flash freezing. The quenched reaction was then mixed with 30 μl of NuPAGE LDS buffer and heated at 95°C for 10 min. Samples were loaded into NuPAGE Novex 4–12% Bis-Tris protein gels (ThermoFisher) run with MES buffer. Gels were

stained with Coomassie Brilliant Blue R-250 (ThermoFisher) and analyzed by quantitative densitometry using Image J.

Single-molecule FRET measurements. FRET measurements of freely diffusing single molecules were performed with a confocal microscope MicroTime 200 (PicoQuant) using published procedures (29, 47). Excitation laser light from 532 nm and 638 nm lasers was used to excite the donor and acceptor fluorophores, respectively. A Pulsed Interleaved Excitation (PIE) setup was used with a pulse rate of 40 MHz to alternate the donor and acceptor excitation. PIE reports the status of both donor and acceptor fluorophores by sorting molecules on the basis of relative donor: acceptor stoichiometry (S) and apparent FRET efficiency (E), as described before (25, 27, 48, 49). A dual band dichroic mirror reflecting 532 and 638 nm guided the light to a high numerical aperture apochromatic objective (60x, N.A. 1.2, water immersion, Olympus) that focused the light to a confocal volume of 1.0 fl for excitation at 532 nm and detection at 575 nm. Fluorescence from excited molecules was collected with the same objective and focused onto a 50-µm diameter pinhole. The donor and acceptor emissions were separated via a dichroic long pass filter with a dividing edge at 620 nm. Suited bandpass filters were inserted to eliminate the respective excitation wavelength and minimize spectral crosstalk. The fluorescence was detected with two avalanche photodiodes using Time-correlated Single Photon Counting with the TimeHarp 200 board. Data were stored in the Time-tagged Time-resolved Mode as a PTU file format. Measurements were performed 25 µm deep in the solution with a total acquisition time of 40 minutes and repeated fresh up to four times on each protein sample (100 pM) in 20 mM Tris, 145 mM NaCl, 2 mM EDTA, 0.003% Tween 20, pH 7.4 (TBSE-T) for oxidized PDI and TBSE-T with 1 mM DTT for reduced PDI. The PDI inhibitors 16F16 (Sigma-Aldrich) and PACMA-31 (Sigma-Aldrich) were added to the solution at a final concentration of 50 µM. Signals from single molecules were observed as bursts of fluorescence. Bursts with more than 40 counts were searched with the All Photon Burst Search (APBS) algorithm while initial integration time was set to 0.5 ms. Appropriate correction for direct excitation of the acceptor at the donor excitation wavelength, leakage of the donor in the acceptor channel, and the instrumental factor was calculated using a mixture of double-stranded DNA models with known FRET efficiency and stoichiometry labeled with dyes Atto-550 and Atto-647N (50). Only molecules with a stoichiometry in the range S=0.25– 0.75 were considered in the final analysis, and their distribution was initially fit to Gaussian curves using Origin 2015 (OriginLab). The number of independent Gaussians was determined according to the corrected Akaike information criterion (AICc). Data recording was performed using the Sympho-Time Software 6.4 (PicoQuant, Berlin). Data analysis was carried out with the Matlab-based software PAM (51). The algorithm used for extracting burst longer than 2 ms was written in the lab using Python.

Acknowledgments. This work was supported in part by grants R01 HL150146 (NP), R01 HL125275 (RF), U01HL143365 (RF) and R35 HL135775 (RF) from the National Heart, Lung and Blood Institute.

Authorship Contributions. M.C., R.F. and N.P. designed the research; M.C. performed the research; M.C., R.F. and N.P. analyzed the data; M.C. R.F. and N.P. wrote the manuscript. All authors reviewed the manuscript.

References

1. C. Klomsiri, P. A. Karplus, L. B. Poole, Cysteine-based redox switches in enzymes. *Antioxid Redox Signal* **14**, 1065-1077 (2011).
2. J. B. Behring *et al.*, Spatial and temporal alterations in protein structure by EGF regulate cryptic cysteine oxidation. *Sci Signal* **13** (2020).
3. J. Chiu, P. J. Hogg, Allosteric disulfides: Sophisticated molecular structures enabling flexible protein regulation. *J Biol Chem* **294**, 2949-2960 (2019).
4. L. Wang, J. Yu, C. C. Wang, Protein disulfide isomerase is regulated in multiple ways: Consequences for conformation, activities, and pathophysiological functions. *Bioessays* 10.1002/bies.202000147, e2000147 (2020).
5. M. Okumura, K. Noi, K. Inaba, Visualization of structural dynamics of protein disulfide isomerase enzymes in catalysis of oxidative folding and reductive unfolding. *Curr Opin Struct Biol* **66**, 49-57 (2020).
6. Y. Wu, D. W. Essex, Vascular thiol isomerases in thrombosis: The yin and yang. *J Thromb Haemost* 10.1111/jth.15019 (2020).
7. E. Lee, D. H. Lee, Emerging roles of protein disulfide isomerase in cancer. *BMB Rep* **50**, 401-410 (2017).
8. M. Matsusaki *et al.*, The Protein Disulfide Isomerase Family: from proteostasis to pathogenesis. *Biochim Biophys Acta Gen Subj* **1864**, 129338 (2020).
9. N. Torpe *et al.*, A Protein Disulfide Isomerase Controls Neuronal Migration through Regulation of Wnt Secretion. *Cell Rep* **26**, 3183-3190 e3185 (2019).
10. L. Schlotawa *et al.*, Recognition and ER Quality Control of Misfolded Formylglycine-Generating Enzyme by Protein Disulfide Isomerase. *Cell Rep* **24**, 27-37 e24 (2018).
11. B. Tsai, C. Rodighiero, W. I. Lencer, T. A. Rapoport, Protein disulfide isomerase acts as a redox-dependent chaperone to unfold cholera toxin. *Cell* **104**, 937-948 (2001).
12. K. Kang, B. Park, C. Oh, K. Cho, K. Ahn, A role for protein disulfide isomerase in the early folding and assembly of MHC class I molecules. *Antioxid Redox Signal* **11**, 2553-2561 (2009).
13. O. Eriksson *et al.*, Thiol isomerase ERp57 targets and modulates the lectin pathway of complement activation. *J Biol Chem* **294**, 4878-4888 (2019).
14. J. Zhou *et al.*, The C-terminal CGHC motif of protein disulfide isomerase supports thrombosis. *J Clin Invest* **125**, 4391-4406 (2015).
15. R. Flaumenhaft, B. Furie, Vascular thiol isomerases. *Blood* **128**, 893-901 (2016).
16. C. Wang *et al.*, Structural insights into the redox-regulated dynamic conformations of human protein disulfide isomerase. *Antioxid Redox Signal* **19**, 36-45 (2013).
17. M. Yagi-Utsumi, T. Satoh, K. Kato, Structural basis of redox-dependent substrate binding of protein disulfide isomerase. *Sci Rep* **5**, 13909 (2015).

18. P. Klappa, L. W. Ruddock, N. J. Darby, R. B. Freedman, The b' domain provides the principal peptide-binding site of protein disulfide isomerase but all domains contribute to binding of misfolded proteins. *EMBO J* **17**, 927-935 (1998).
19. G. Tian, S. Xiang, R. Noiva, W. J. Lennarz, H. Schindelin, The crystal structure of yeast protein disulfide isomerase suggests cooperativity between its active sites. *Cell* **124**, 61-73 (2006).
20. L. Peng, M. I. Rasmussen, A. Chailyan, G. Houen, P. Hojrup, Probing the structure of human protein disulfide isomerase by chemical cross-linking combined with mass spectrometry. *J Proteomics* **108**, 1-16 (2014).
21. R. A. Romer *et al.*, The flexibility and dynamics of protein disulfide isomerase. *Proteins* **84**, 1776-1785 (2016).
22. R. B. Freedman *et al.*, 'Something in the way she moves': The functional significance of flexibility in the multiple roles of protein disulfide isomerase (PDI). *Biochim Biophys Acta Proteins Proteom* **1865**, 1383-1394 (2017).
23. M. Okumura *et al.*, Dynamic assembly of protein disulfide isomerase in catalysis of oxidative folding. *Nat Chem Biol* **15**, 499-509 (2019).
24. H. Y. Aviram *et al.*, Direct observation of ultrafast large-scale dynamics of an enzyme under turnover conditions. *Proc Natl Acad Sci U S A* **115**, 3243-3248 (2018).
25. A. Barth *et al.*, Dynamic interactions of type I cohesin modules fine-tune the structure of the cellulosome of Clostridium thermocellum. *Proc Natl Acad Sci U S A* **115**, E11274-E11283 (2018).
26. H. Mazal *et al.*, Tunable microsecond dynamics of an allosteric switch regulate the activity of a AAA+ disaggregation machine. *Nat Commun* **10**, 1438 (2019).
27. A. C. Ferreon, C. R. Moran, Y. Gambin, A. A. Deniz, Single-molecule fluorescence studies of intrinsically disordered proteins. *Methods Enzymol* **472**, 179-204 (2010).
28. F. Sturzenegger *et al.*, Transition path times of coupled folding and binding reveal the formation of an encounter complex. *Nat Commun* **9**, 4708 (2018).
29. M. Chinnaraj *et al.*, Bioorthogonal Chemistry Enables Single-Molecule FRET Measurements of Catalytically Active Protein Disulfide Isomerase. *Chembiochem* 10.1002/cbic.202000537 (2020).
30. S. Kalinin, A. Valeri, M. Antonik, S. Felekyan, C. A. Seidel, Detection of structural dynamics by FRET: a photon distribution and fluorescence lifetime analysis of systems with multiple states. *J Phys Chem B* **114**, 7983-7995 (2010).
31. I. V. Gopich, A. Szabo, Theory of the energy transfer efficiency and fluorescence lifetime distribution in single-molecule FRET. *Proc Natl Acad Sci U S A* **109**, 7747-7752 (2012).
32. H. Sanabria *et al.*, Resolving dynamics and function of transient states in single enzyme molecules. *Nat Commun* **11**, 1231 (2020).
33. I. V. Gopich, A. Szabo, Single-molecule FRET with diffusion and conformational dynamics. *J Phys Chem B* **111**, 12925-12932 (2007).

34. Y. Santoso *et al.*, Conformational transitions in DNA polymerase I revealed by single-molecule FRET. *Proc Natl Acad Sci U S A* **107**, 715-720 (2010).
35. B. G. Hoffstrom *et al.*, Inhibitors of protein disulfide isomerase suppress apoptosis induced by misfolded proteins. *Nat Chem Biol* **6**, 900-906 (2010).
36. S. Xu *et al.*, Discovery of an orally active small-molecule irreversible inhibitor of protein disulfide isomerase for ovarian cancer treatment. *Proc Natl Acad Sci U S A* **109**, 16348-16353 (2012).
37. R. H. Bekendam *et al.*, A substrate-driven allosteric switch that enhances PDI catalytic activity. *Nat Commun* **7**, 12579 (2016).
38. N. J. Darby, T. E. Creighton, Functional properties of the individual thioredoxin-like domains of protein disulfide isomerase. *Biochemistry* **34**, 11725-11735 (1995).
39. C. Wang *et al.*, Human protein-disulfide isomerase is a redox-regulated chaperone activated by oxidation of domain a'. *J Biol Chem* **287**, 1139-1149 (2012).
40. U. Woehlbier *et al.*, ALS-linked protein disulfide isomerase variants cause motor dysfunction. *EMBO J* **35**, 845-865 (2016).
41. C. Wang *et al.*, Plasticity of human protein disulfide isomerase: evidence for mobility around the X-linker region and its functional significance. *J Biol Chem* **285**, 26788-26797 (2010).
42. B. Nguyen, Y. Ordabayev, J. E. Sokoloski, E. Weiland, T. M. Lohman, Large domain movements upon UvrD dimerization and helicase activation. *Proc Natl Acad Sci U S A* **114**, 12178-12183 (2017).
43. I. Grossman *et al.*, Single-molecule spectroscopy exposes hidden states in an enzymatic electron relay. *Nat Commun* **6**, 8624 (2015).
44. K. Henzler-Wildman, D. Kern, Dynamic personalities of proteins. *Nature* **450**, 964-972 (2007).
45. T. Xie, T. Saleh, P. Rossi, C. G. Kalodimos, Conformational states dynamically populated by a kinase determine its function. *Science* **370** (2020).
46. R. Otten *et al.*, How directed evolution reshapes the energy landscape in an enzyme to boost catalysis. *Science* 10.1126/science.abd3623 (2020).
47. E. Ruben *et al.*, The J-elongated conformation of beta2-glycoprotein I predominates in solution: implications for our understanding of antiphospholipid syndrome. *J Biol Chem* **295**, 10794-10806 (2020).
48. V. Kudryavtsev *et al.*, Combining MFD and PIE for accurate single-pair Forster resonance energy transfer measurements. *Chemphyschem* **13**, 1060-1078 (2012).
49. A. N. Kapanidis *et al.*, Fluorescence-aided molecule sorting: analysis of structure and interactions by alternating-laser excitation of single molecules. *Proc Natl Acad Sci U S A* **101**, 8936-8941 (2004).
50. B. Hellenkamp *et al.*, Precision and accuracy of single-molecule FRET measurements-a multi-laboratory benchmark study. *Nat Methods* **15**, 669-676 (2018).

51. W. Schrimpf, A. Barth, J. Hendrix, D. C. Lamb, PAM: A Framework for Integrated Analysis of Imaging, Single-Molecule, and Ensemble Fluorescence Data. *Biophys J* **114**, 1518-1528 (2018).
52. M. Dimura *et al.*, Automated and optimally FRET-assisted structural modeling. *Nat Commun* **11**, 5394 (2020).

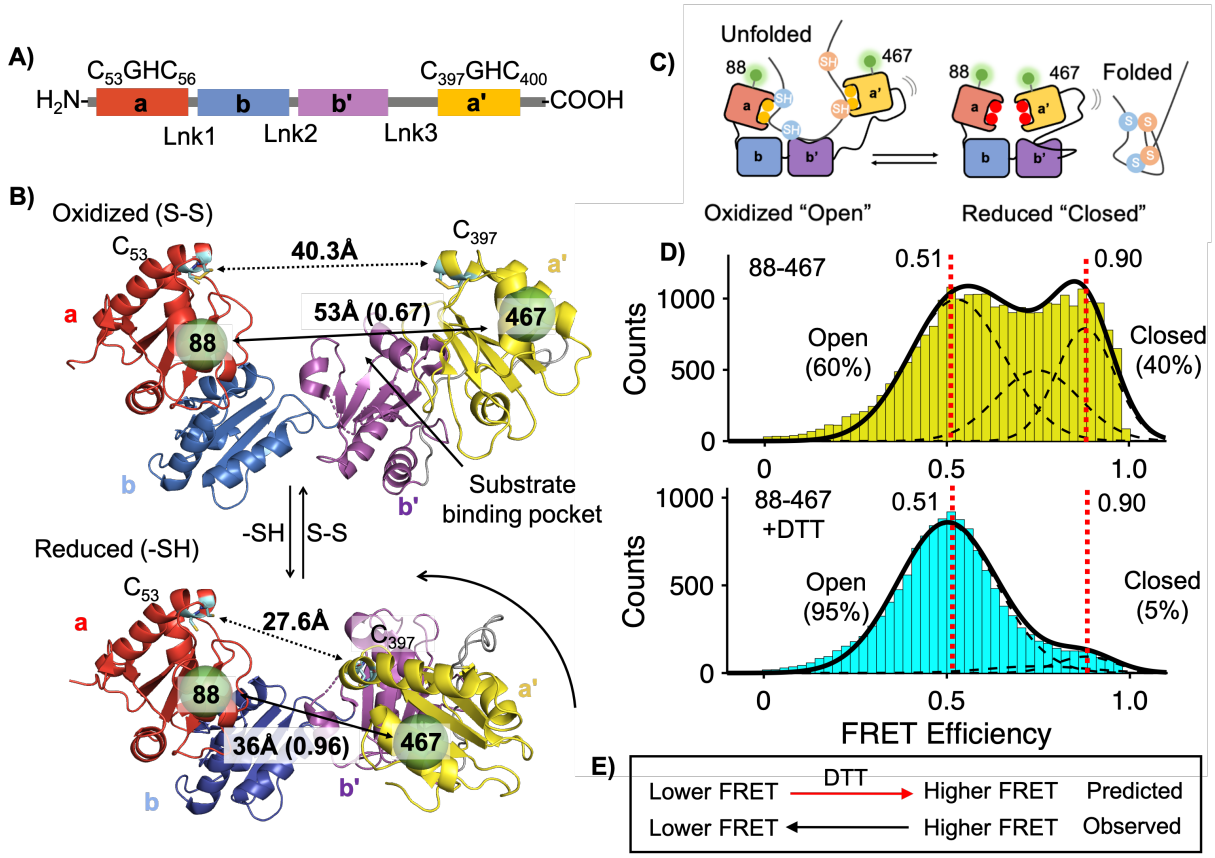

Figure 1. smFRET studies of human PDI. A) Domain structure of human PDI. PDI comprises 508 AA organized in four domains, **a** (18-133, red), **b** (138-232, blue), **b'** (magenta, 237-348) and **a'** (370-479, yellow), connected by three flexible linkers, Lnk1 (134-137), Lnk2 (233-236) and Lnk3 (349-369, also known as the **x**-linker). Domains **a** and **a'** contain the active sites CGHC. **B)** Top view of the X-ray crystal structures of oxidized (S-S, top panel, 4el1) and reduced (SH, bottom panel, 4ekz) PDI documenting a U-shape architecture and inward movement of the **a'** domain (yellow) toward the **b'** domain (magenta) upon reduction of the active sites to occlude the substrate binding pocket (indicated with an arrow in the top panel). Shown as dotted lines are the distances between the active sites. The green spheres represent residues S88 and K467. Shown as lines are the Cβ-Cβ distances between residues S88 and K467 and, in parenthesis, are the values of energy transfer estimated with the software FPS (52) and a value of R_0=65Å for the FRET pair Atto-550/467N. **C)** Structure-based conformational cycle for PDI inferred by X-ray crystallography. In the oxidized form, PDI adopts an open conformation primed for substrate binding due to the large distance between the **a** and **a'** domains and exposure of the substrate binding pocket in the **b'** domain. By contrast, in the reduced form, PDI adopts a closed conformation. This conformation can no longer accommodate a folded substrate, which is released. The location of residues S88 and K467 is shown in green. **D)** FRET efficiency histograms of PDI 88/467 obtained in the absence (yellow, top panel) and presence (cyan, bottom panel) of 1 mM DTT fit with three Gaussians (χ^2=2.71) (black lines) signifying the presence of two major conformational ensembles, open and closed, and the transition between them. The fraction (%) for each population is reported in parenthesis. The vertical red lines in each graph indicates the mean value of transfer efficiency calculated for the open and closed ensemble. **E)** Disagreement between theoretical and experimentally determined FRET trends in PDI 88/467. In the presence of DTT, the signal shifts towards lower FRET values and not higher, as predicted by **panel B**, documenting redox-dependent conformational changes leading to stabilization of the open state.

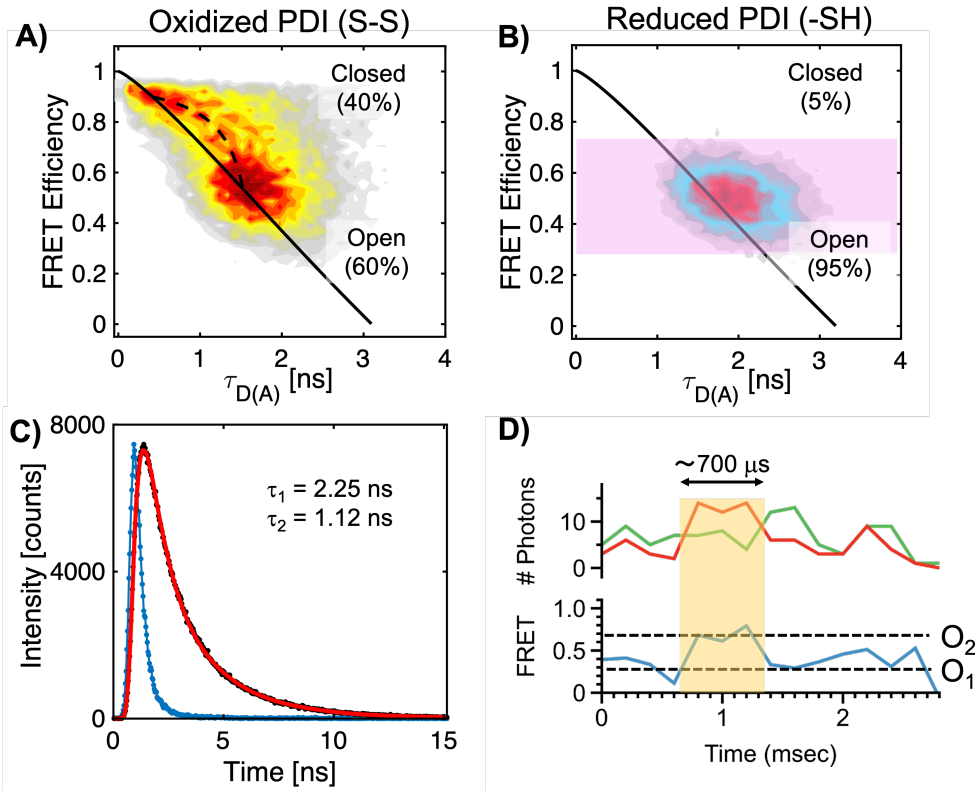

Figure 2. Dynamics of oxidized and reduced PDI. Shown are the two-dimensional plots of FRET efficiency (y-axis) versus lifetime of the donor in the presence of the acceptor $\tau_{D(A)}$ (x-axis) for **(A)** oxidized and **(B)** reduced PDI 88/467 documenting the dynamic exchange between closed (high FRET) and open (low FRET) ensembles occurring in the millisecond timescale. The solid black line describes the theoretic relationship between FRET and lifetime. The systematic deviation from this relationship highlighted by the dotted line tracks the trajectory of single molecules that are exchanging between high and low FRET states while passing through the confocal volume. The fraction (%) of closed and open ensembles at equilibrium is reported according to the values obtained in **figure 1D**. The magenta region in **panel B** indicates the molecules selected for the lifetime analysis (0.25-0.65) shown in panel B. **C)** Subpopulation specific fluorescence lifetime of reduced PDI 88/467. Data points are in black. The red line represents the best fit obtained with a double exponential function (χ^2=1.21). The value of lifetime of each population is shown. The instrumental response function is shown in blue. **D)** smFRET trajectory of a single PDI 88/467 molecule traversing the confocal volume. Top panel shows donor (green) and acceptor (red) signals binned in 200 µs bins. Bottom panel shows the calculated FRET efficiency (blue). The yellow region indicates a transition between O_1 (E_1=0.35) and O_2 (E_2=0.7). In this event, PDI 88/467 remains in the O_1 state for ~700 µs.

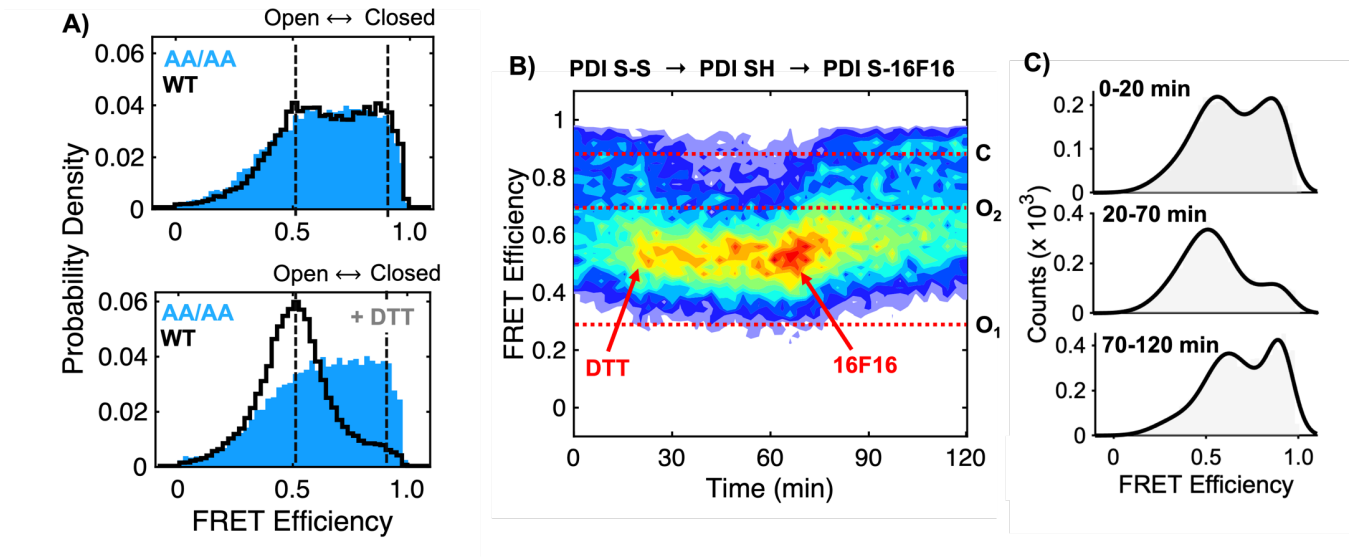

Figure 3. Free thiols stabilize the open ensemble. A) Normalized FRET efficiency histograms of PDI 88/467 C53A/C56A/C397A/C400A (AA/AA, blue) overlaid to PDI WT (black) before (top panel) and after (bottom panel) the addition of 1 mM DTT. The vertical lines indicate the FRET values for the closed and open states. Note how PDI AA/AA is similar to oxidized PDI WT and insensitive to DTT. **B)** Real-time monitoring of PDI conformational cycle. A solution of oxidized PDI 88/467 was continuously monitored for 120 min under different experimental conditions to follow the conformational changes associated with reduction of the active site cysteines to thiol groups by DTT and then their alkylation by the compound 16F16. DTT (50 μM) was added after 20 min. 16F16 (50 μM) was added after 70 min. Addition of DTT and 16F16 is indicated with red arrows. The mean FRET efficiency value of closed **(C)** and open (O_1 and O_2) states identified by our previous analysis is shown on the right. As expected, oxidized PDI 88/467 visits closed and open ensembles with similar probability, and addition of DTT shifts the equilibrium toward lower FRET values. Addition of 16F16 to reduced PDI shifts the equilibrium back to the closed ensemble. **C)** FRET efficiency histograms of PDI 88/467 at different time intervals corresponding to the reaction of PDI 88/467 with 16F16 shown in **panel B**.

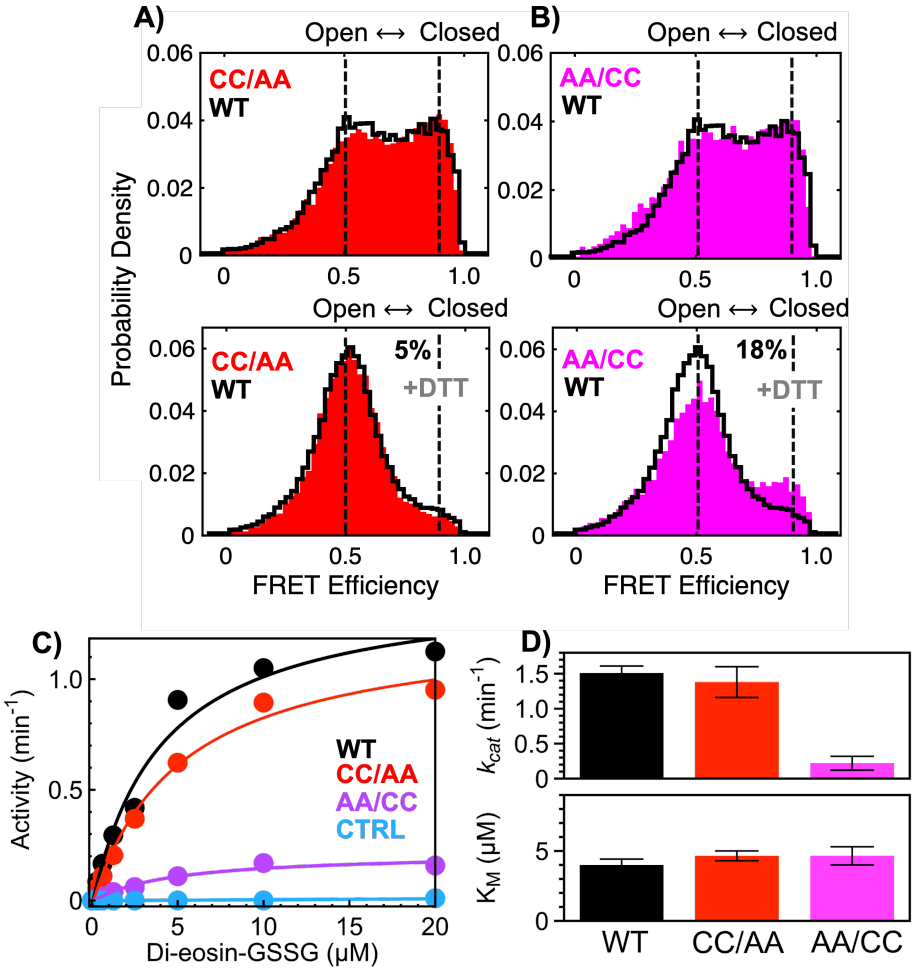

Figure 4. Structural and functional nonequivalence of the active sites. Normalized FRET efficiency histograms of **(A)** PDI 88/467 C397A/C400A (CC/AA, red) and **(B)** PDI C53A/C56A (AA/CC, magenta) overlaid to PDI WT (black) before (top panel) and after (bottom panel) the addition of 1 mM DTT. The vertical lines indicate the FRET values for the closed and open states. Note how the mutations C53A and C56A led to a macroscopic accumulation of the closed state, which increased more than 3-times, from 5% to 18%. **C)** Reductase activity of the PDI 88/467 (WT, black) and active site variants PDI AA/AA (blue), PDI CC/AA (red) and PDI AA/CC (magenta) monitored by the di-eosin GSSG assay. Best fit obtained with the Michaelis-Menten equation are shown as solid lines. **D)** Turnover number (k_{cat} in min^{-1}) and apparent affinity constant for the substrate di-eosin GSSG (K_M in μM) calculated in **panel C**.

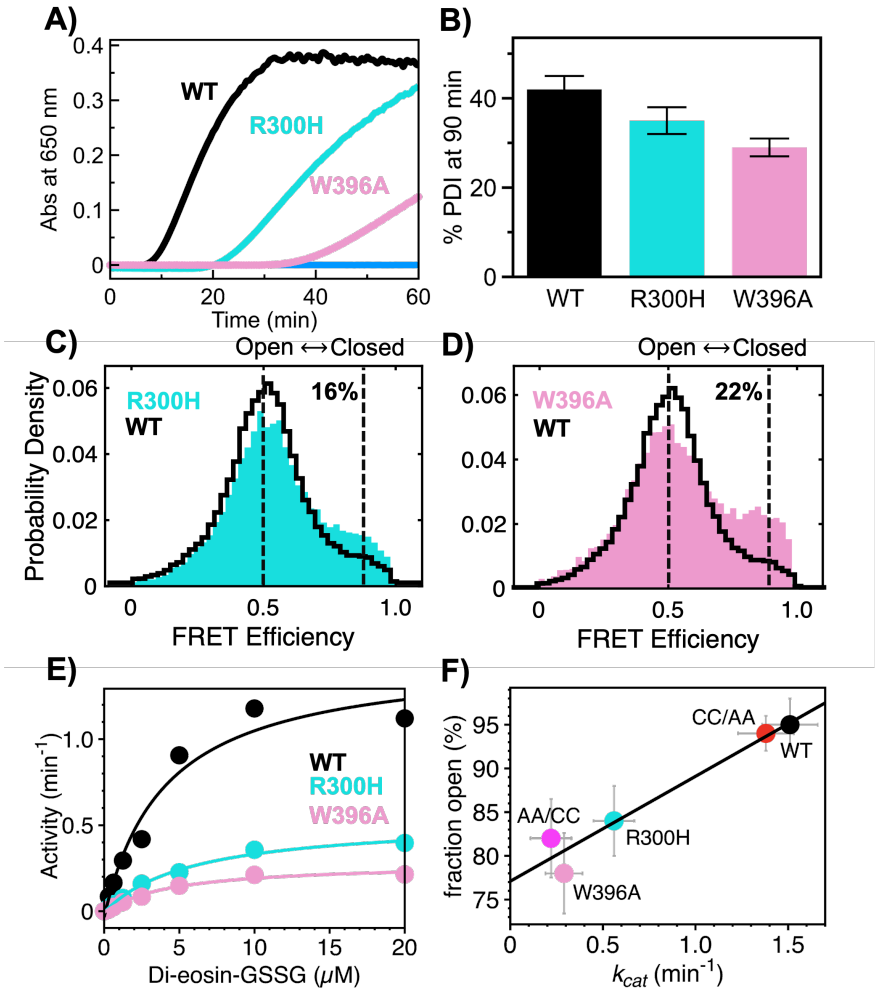

Figure 5. Destabilization of the open conformation results in decreased reductase activity of PDI. **A)** Reductase activity of PDI 88/467 (WT) and mutants PDI 88/467 R300H (R300H) and PDI 88/467 W396A (W396A) measured using the insulin assay. Inactive PDI AA/AA (blue) was used as a negative control. **B)** Limited proteolysis of PDI by proteinase K. Shown is the percent of intact PDI measured after 90 min of reaction, which was monitored by SDS-PAGE. The original gel corresponding to this panel is shown in **Figure S5** in the Supplementary Information. Normalized FRET efficiency histograms of reduced **(C)** PDI 88/467/R300H (cyan) and **(D)** PDI 88/467/W396A (magenta) overlayed with PDI WT (black) document a significant shift toward the closed ensemble. **E)** Kinetic plots of PDI 88/467 (black), PDI 88/467/R300H (cyan) and PDI 88/467/W396A (magenta) obtained by increasing the concentration of di-eosin-GSSG. **F)** Percent (%) fraction of PDI open plotted against turnover values (k_{cat}, min^{-1}) obtained from the kinetic analysis of di-eosin-GSSG cleavage for the PDI variants produced in this study. The correlation coefficient (R^2) of the line interpolating the data is 0.94.

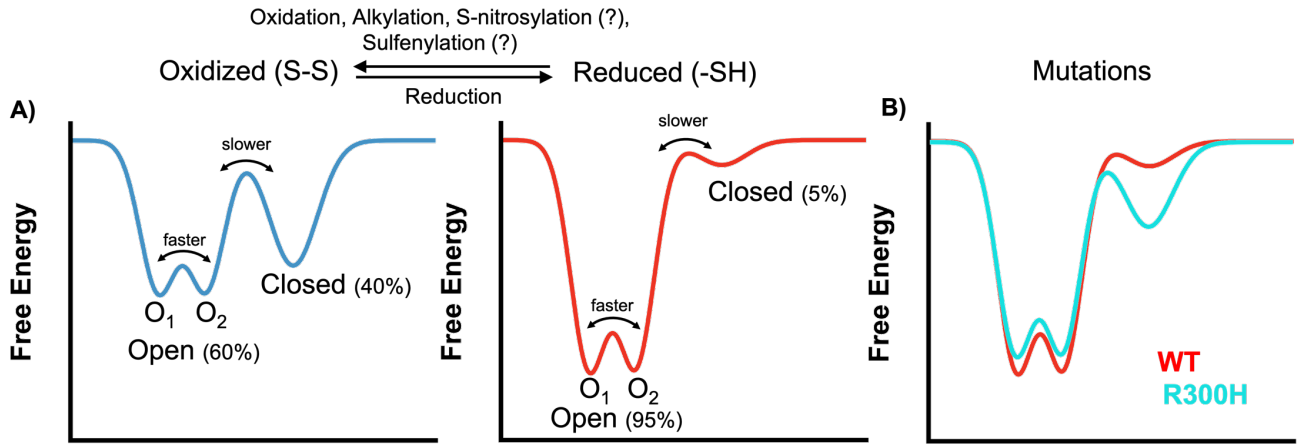

Figure 6. Summary of PDI's conformational cycle obtained by smFRET. (A) Shown is the free energy landscape for oxidized (left) and reduced (right) PDI depicting the distribution of each state at equilibrium. Perturbation of this equilibrium by environmental factors like oxidative stress, alkylation, S-nitrosylation, and sulfenylation and **(B)** single point mutations disrupts PDI activity.

Supplementary Information

A cysteine-based redox switch regulates millisecond dynamics of PDI and controls enzyme activity

Mathivanan Chinnaraj[1], Robert Flaumenhaft[2,*] and Nicola Pozzi[1,*]

[1]Edward A. Doisy Department of Biochemistry and Molecular Biology, Saint Louis University School of Medicine, St. Louis, MO, 63104, USA.
[2]Division of Hemostasis and Thrombosis, Department of Medicine, Beth Israel Deaconess Medical Center, Harvard Medical School, Boston, Massachusetts 02115, USA.

Table of Contents

Table S1. Anisotropy and quantum yield (**Φ**) values for singly labeled PDI mutants.

Figure S1. Structural and functional characterization of doubly labelled PDI.

Figure S2. Rapid microsecond timescale movements of the **a** and **a'** domains in the open ensemble.

Figure S3. Functional characterization of the active site mutant PDI C53A/C56A/C397A/C400A.

Figure S4. Structural perturbation of the reduced state caused by PACMA-31 monitored by smFRET.

Figure S5. Limited proteolysis of PDI by proteinase K followed by SDS-PAGE.

Table S1. Anisotropy and quantum yield (**Φ**) values for singly labeled PDI mutants.

Construct	**Atto-550** anisotropy	**Atto-550** **Φ**	**Atto-647N** anisotropy	**Atto-647N** **Φ**
S88U	0.19±0.02	0.79±0.02	0.18±0.02	0.65±0.02
K467U	0.21±0.02	0.79±0.02	0.21±0.02	0.65±0.02

Experimental conditions are 100 mM potassium phosphate (pH 7.4), 2 mM EDTA, at 25°C. For anisotropy determination, the concentration of PDI was 10 nM, ex 540/em580 for Atto-550 and ex640/em680 for Atto-647N, ex/em slits 1 and 14 nm, respectively. The results represent the average of two independent determinations. For quantum yield determination Rhodamine 110 (Φ=0.89±0.02) in ethanol was used as a standard, for free dyes in buffer, Atto-550 (Φ=0.79±0.02) and Atto-647N (Φ=0.64±0.02) were also experimentally determined.

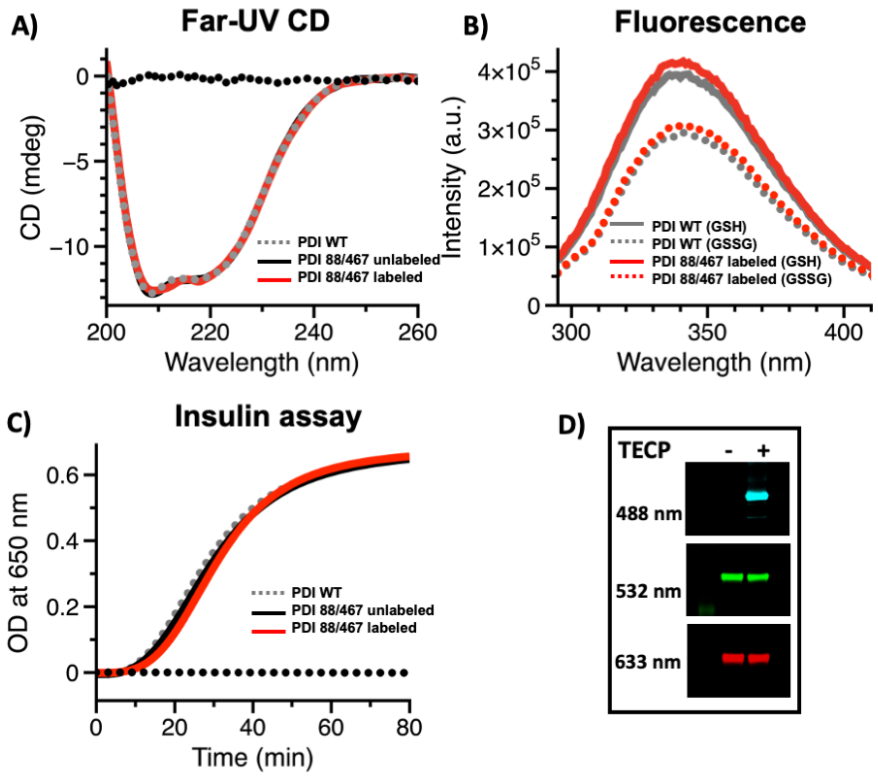

Figure S1. Structural and functional characterization of doubly labelled PDI. A) Far-UV CD spectra of PDI WT (gray dotted line), unlabeled (black) and fluorescently labelled (red) PDI 88/467 obtained in 100 mM potassium phosphate (pH 7.4), 2 mM EDTA, at 25°C. Buffer only is shown as a black dotted line. **B)** Fluorescence spectra of PDI WT (200 nM, black) and fluorescently labelled PDI 88/467 (200 nM, red) obtained under reducing (1 mM GSH, solid lines) and oxidizing (1 mM GSSG, dotted lines) conditions. **C)** Reductase activity of PDI monitored by the insulin assay. Shown are the progress curves for PDI WT (gray) and PDI 88/467 before (black) and after labeling (red). No absorbance at 650 nm was observed in the absence of enzyme (black dotted line). **D)** Reactivity of monomeric doubly labeled PDI 88/467 (5 μM) toward AlexaFluor-488 maleimide (25 μM, top panel) in the absence (-) and in the presence of the thiol reducing agent TCEP (+, 500 μM). The gel was sequentially irradiated with 488-nm, 532-nm and 633-nm lasers to document the incorporation of AlexaFluor-488, Atto-550 and Atto-647N.

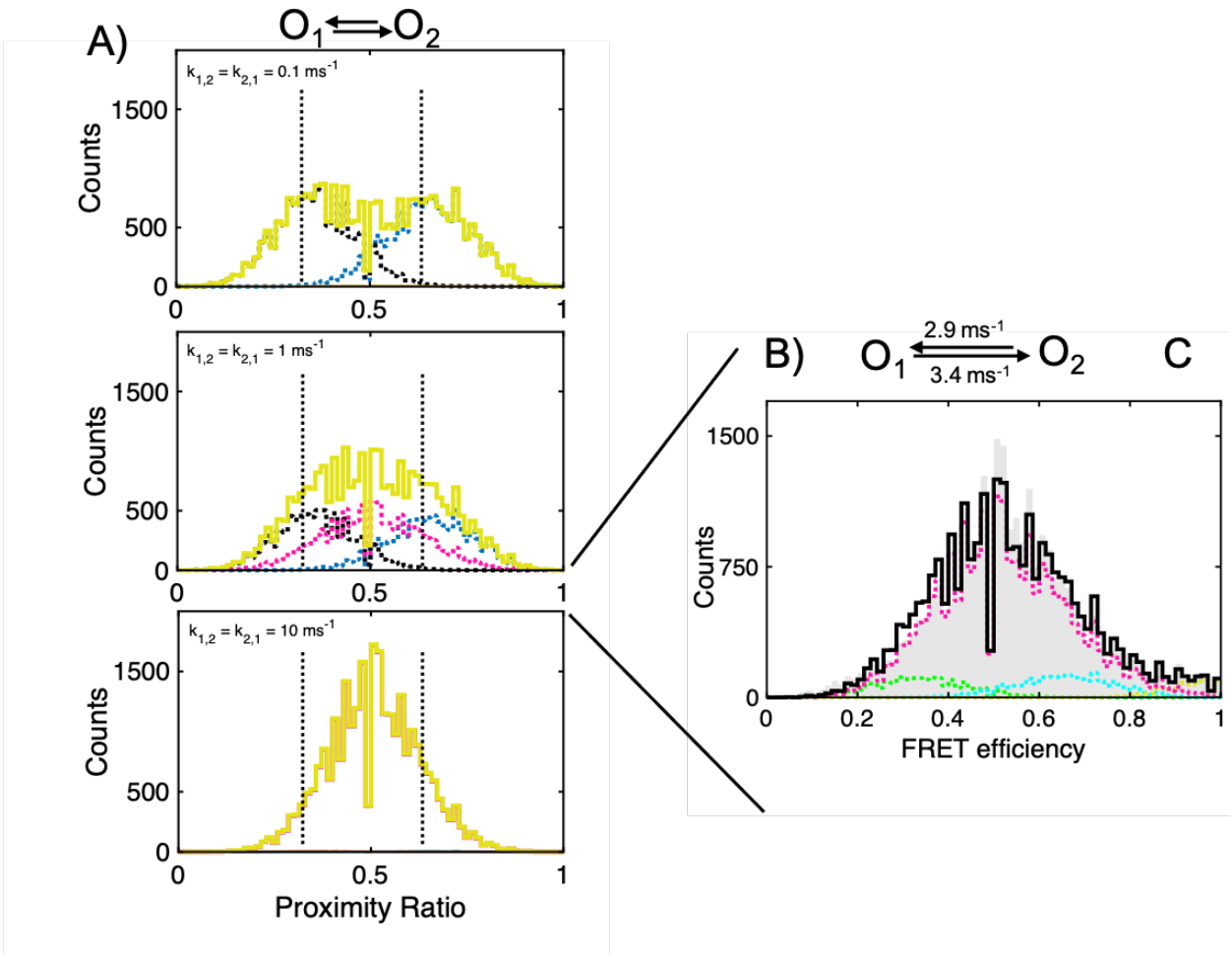

Figure S2. Rapid microsecond timescale movements of the a and a' domains in the open ensemble. (A) Simulated behavior of a dynamic two-state system, E=0.35 (O_1) and E=0.7 (O_2) in which the interconversion rates varies 100-fold, from 0.1 ms^{-1} (top panel) to 10 ms^{-1} (bottom panel). As the interconversion rates increase, the two states progressively merge to form one peak centered at E=0.5. Merging starts at 1 ms^{-1} and is completed at 10 ms^{-1}. This data indicates that O_1 and O_2 exchange faster than 1 ms^{-1} but slower than 10 ms^{-1}. **(B)** Considering that approximately 5% of reduced PDI 88/467 visits the closed conformation, probability distribution analysis (PDA) was performed on the dataset of reduced PDI 88/467 to estimate the interconversion rate constants. Using a dynamic two-state model with the addition of a static high FRET population, which represents the closed conformation, we obtained interconversion rate constants $k_{1,2}$=3.4 ms^{-1} and $k_{2,1}$=2.9 ms^{-1}, which agrees with the simulations and correspond to dwell times of ~290 μs for O_1 and ~350 μs for O_2.

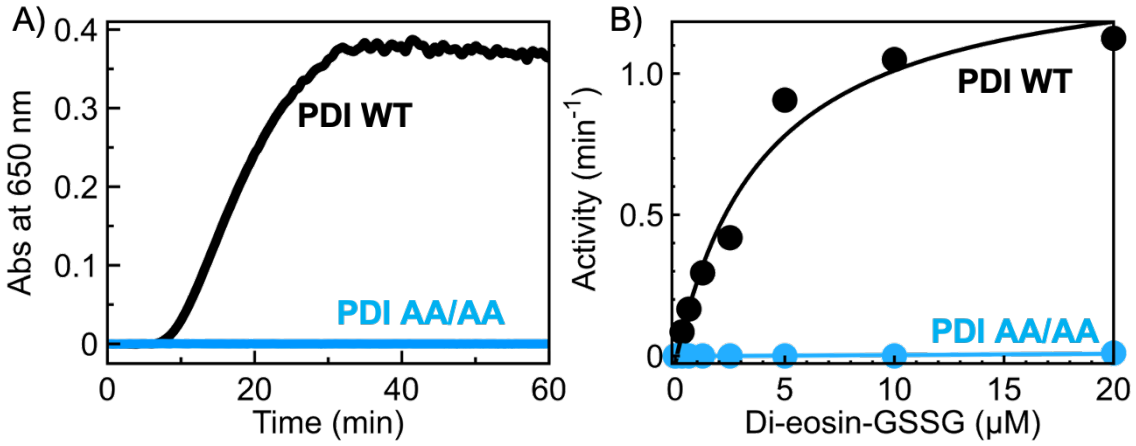

Figure S3. Functional characterization of the active site mutant PDI C53A/C56A/C397A/C400A (PDI AA/AA). Reductase activity of PDI WT (black) and PDI AA/AA (blue) monitored by the **(A)** insulin reductase assay and **(B)** di-eosin-GSSG assay. No catalytic activity was recorded for PDI AA/AA.

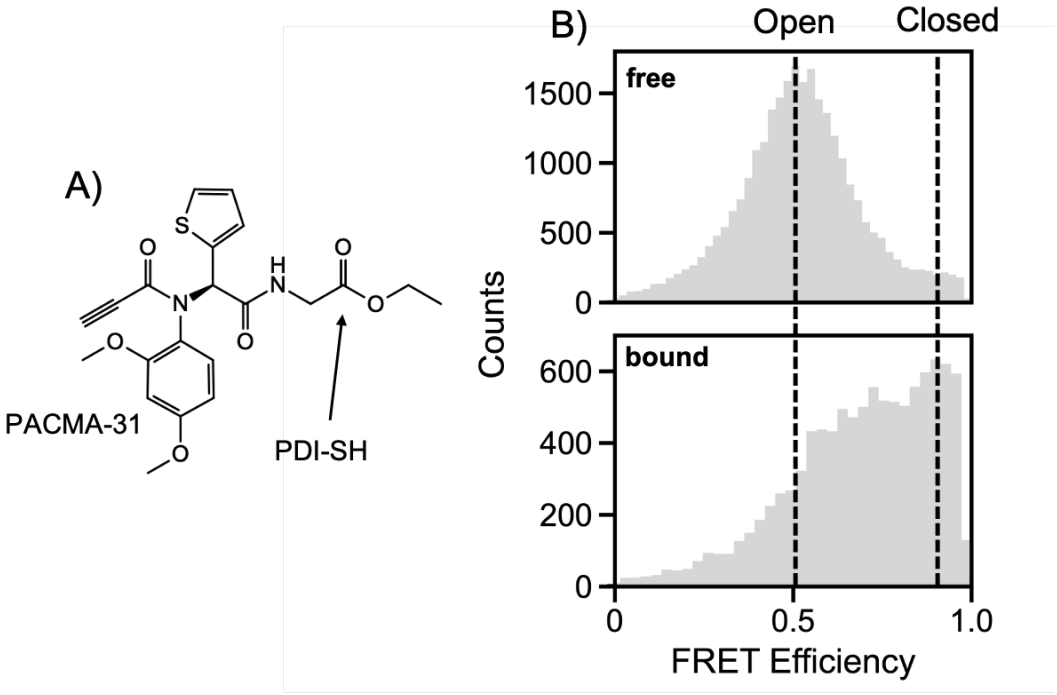

Figure S4. Structural perturbation of the reduced state caused by PACMA-31 monitored by smFRET. (A) Because of the electron-deficient nature of the propynoic acid amide moiety PACMA-31 reacts irreversibly with the active site thiol groups of PDI to form a covalent adduct. **(B)** FRET histograms of PDI 88/467 (100 pM, TBSE-T) in the presence of DTT (1 mM) before (free, top panel) and after (bound) the addition of 50 μM PACMA-31. Note how PACMA-31 shifts the conformational equilibrium towards the closed ensemble.

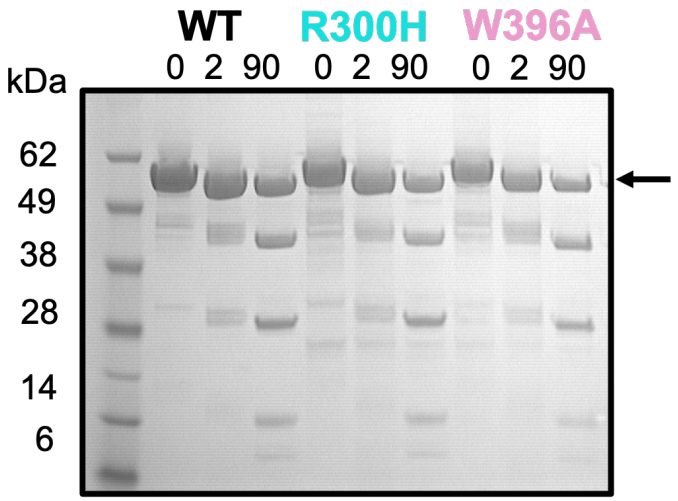

Figure S5. Limited proteolysis of PDI by proteinase K followed by SDS-PAGE. Limited proteolysis of PDI 88/467 (WT) and mutants R300H (cyan) and W396A (magenta) at 1 mg/ml by proteinase K (5 μg/ml) performed under reducing conditions (1 mM DTT). PDI was solubilized in the same buffer used for the smFRET experiment, and after addition of the enzyme, the reaction was quenched with 1 mM PMSF at 2 and 90 min. The arrow indicates intact PDI.